Modeling of Pneumatic Melt Spinning Processes

Leszek Jarecki, Slawomir Blonski, Anna Blim, Andrzej Zachara

Institute of Fundamental Technological Research, Polish Academy of Sciences, Pawinskiego 5B, Warsaw 02-106, Poland

Received 30 November 2011; accepted 30 November 2011
DOI 10.1002/app.36575
Published online in Wiley Online Library (wileyonlinelibrary.com).

ABSTRACT: Computer simulation of the pneumatic processes of fiber formation from the polymer melts is discussed. The dynamics of air-drawing of thin polymer streams in supersonic air jets formed in the Laval nozzle is presented versus the melt blowing process. In the Laval nozzle process, the air flow takes place with high Reynolds number and the k–ω model is used which considers kinetic energy of the air flow and the specific dissipation rate of the kinetic energy. For melt blowing, the air fields are simulated with the use of the k–ε turbulent model. The air velocity, temperature, and pressure distributions along the centerline of the air jets are considered in the modeling of both pneumatic processes. The air fields are predetermined at the absence of the polymer streams for several air compression values in the Laval nozzle inlet and several initial air velocities in the melt blowing process. Each polymer stream in a usual configuration of a single row of the filaments in the process is considered as non-interacting aerodynamically with other streams, and the air jet is assumed to be undisturbed by the polymer streams. Air-drawing of the polymer filaments is simulated as controlled by the distribution of air velocity, temperature, and pressure on the air jet centerline with the use of a stationary model of melt spinning in a single-, thin-filament approximation. Effects of non-linear viscoelasticity of the polymer melt subjected to fast uniaxial elongation are accounted for in the modeling. Strong influence of the air jet velocity, the melt viscosity which controls response of the polymer melt on the air-drawing forces, and the die-to-collector distance has been predicted. Influence of initial air temperature, geometry of the air die, initial velocity and temperature of the melt, extrusion orifice diameter can be also predicted from the model. The example computations concern air-drawing of isotactic polypropylene with the use of the Laval nozzle are compared with the predictions for the melt blowing process. © 2012 Wiley Periodicals, Inc. J Appl Polym Sci 000: 000–000, 2012

Key words: computer modeling; fibers; melt blowing; supersonic melt spinning; polypropylene

INTRODUCTION

Pneumatic methods of melt spinning, i.e., melt blowing and air-drawing with the use of Laval nozzle, provide an efficient way of obtaining super-thin fibers from a variety of thermoplastic fiber-forming polymers in which web structure is obtained in a one-step process. Nowadays, the interest in the laboratory research and technology of fabrication of ultra-fine fibers results from an increasing demand of high-surface-activity fabrics designed for technical, biotechnological, and medical applications, such as filtration and germicide mats, medical implants, tissue engineering scaffolds, non-wovens with surface catalyzers, enzymes etc. Such products take advantage of high specific surface of ultra-fine fibers, inversely proportional to their diameter. Ultra-fine fibers with high molecular orientation could find application also in the reinforcement of composites.

Super-thin fibers are defined as fibers with the diameter in the range 10–0.1 μm, with the specific surface in the range 0.4–40 m^2/cm^3 (Fig. 1). They are thinner than those obtained in high-speed melt spinning. Higher specific fiber surface of the order of 100 m^2/cm^3 is obtained by electrospinning. The method allows to obtain filaments with the diameter as small as 50 nm, but it usually involves solvents and the output is by orders of magnitude lower.

Commercial non-wovens of fibers with the diameter as small as 1–2 μm are now produced by a number of companies with the use of melt blowing technology. In melt blowing, two convergent high-velocity jets of hot air are blown from rectangular air slots on both sides of a longitudinal spinning beam onto the polymer filaments. Due to frequent online brakes of the air-drawn filaments taking place in melt blowing under stochastic coiling and entanglements, finite length fibers, often very short, are produced by this method.[1–4] Besides, melt blowing involves high volumes of hot air resulting in high energy consumption and requires manufacturing of high precision die assembly.[5]

Correspondence to: L. Jarecki (ljarecki@ippt.gov.pl).
Contract grant sponsor: Ministry of Science and Higher Education of the Republic of Poland; contract grant number: N N507 448437.

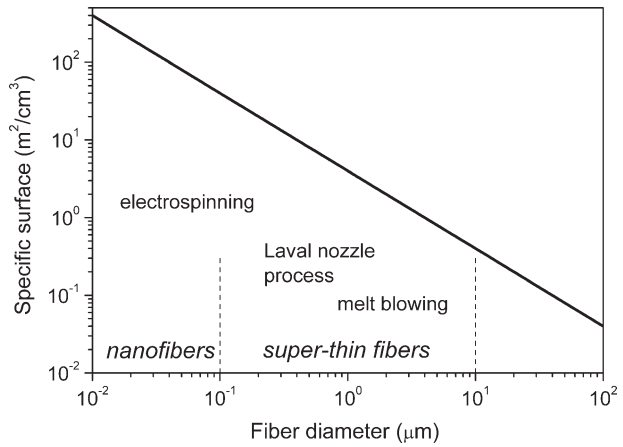

Figure 1 Specific surface of fibers versus fiber diameter and the thickness ranges of fibers obtained by different methods.

A new and efficient pneumatic process has been invented in this decade in the Nanoval Company in Berlin with the application of Laval nozzle where the streams of fiber-forming polymers are melt drawn in the supersonic air jet.[6–8] In this process, cold air is used to generate supersonic air jet, and the polymer streams extruded coaxially with the air jet undergo very rapid pneumatic drawing to super-thin fibers. Air velocity in the supersonic Laval nozzle process is not decelerating away from the nozzle, as it is in melt blowing, and continuous fibers are successfully obtained. Also the design and use of the die assembly is simpler due to not so fine dies needed in the process.[6,9] Gerking[6–8] claims that the polymer melt monofilaments are attenuated in the Laval nozzle by the supersonic air jet until they disintegrate into a number of sub-filaments by a longitudinal burst splitting. However, observation of the splitting is controversial and some other authors do not observe the fiber splitting phenomena in the process. Mechanism involved in the burst opening of the filaments, as well as dynamics of the supersonic air-drawing of the melt are not clear.

Experimental tests on melt drawing of polypropylene in the Laval nozzle indicate that higher air pressure used in the nozzle inlet leads to finer filaments in the non-wovens' structure due to higher air jet velocity along the spinline. It is confirmed that the supersonic process is effective for production of continuous fine fibers at the compression of the air in the nozzle inlet around one bar, or more. Nevertheless, the scanning electron microscope (SEM) observations of the polypropylene non-wovens do not indicate burst splitting of the air-drawn monofilaments.[10,11] The SEM images show polypropylene fibers with smooth surface and uniform diameter, without irregularities in the shapes, cracks, or splitting. Burst splitting is a random process and one should expect the irregularities, as well as broad distribution of the fibers' diameter. Also model considerations are still lacking in the literature which would describe dynamics of the Laval nozzle process.

Pneumatic processes of melt spinning are complicated by the influence of relatively high number of the process parameters, coupled with the influence of material parameters of the polymer. In this article, we compare influence of important process and material parameters on the dynamics of the melt air-drawing in the supersonic Laval nozzle process with that in melt blowing. The comparison bases on the results obtained from computations performed using fundamental equations of mathematical model of melt spinning adopted for air-drawing of the melt in a coaxial air jet. The aerodynamic model of the air jet will be applied for the Laval nozzle process taking into account supersonic air velocities, as well as the latest model of rapid extension of a thin stream of the melt in a coaxial air jet.[12,13]

MODEL APPROXIMATIONS

In both pneumatic processes, melt blowing and the Laval nozzle process, the die assembly is usually longitudinal and consists of a longitudinal spinneret with a single row of melt extrusion orifices with circular cross-section and a longitudinal air die symmetrically on both sides of the orifices. The curtain of thin polymer streams extruded from the orifices in the symmetry plane of the air jet is subjected to rapid drawing by the air flowing along the streams.[2,6] The fibers fall down freely onto a collector at a fixed distance from the spinneret forming a web of statistically distributed fibers.

In the Laval nozzle process, velocity of the air jet achieves supersonic level within the nozzle and remains at such level over a considerable range of the process axis what results in continuous filaments deposited into the web. In melt blowing, deceleration of the air jet along the process axis leads to intensive coiling, entanglements, and breaks of the filaments before they achieve the collector, starting form the point where the filament and the air velocities coincide. Differences in the dynamics of the air jets in the melt blowing and Laval nozzle processes is reflected in the dynamics of air-drawing of the melt, as well as in the non-wovens' structure. Computer modeling is used in this article to illustrate differences in the character of both processes and show influence of important processing and material parameters on the main features of the processes.

For longitudinal die assemblies, with the aspect ratio exceeding 50, modeling of the process dynamics reduces to two dimensions in the cross-section plane normal to the long dimension of the die

assembly. In both pneumatic processes, thin polymer filaments are extruded along the symmetry axis of the air jet in the plane, z, and the problem reduces to two-dimensional air jet blown symmetrically on both sides of each filament. The melt extrusion velocity, V_0, is constant for stationary processes and the filaments attenuated by the aerodynamic forces along the z-axis fall down onto the collector at a fixed distance from the extrusion point, L. In melt blowing, initial velocity of hot air at the exit of the air slots is in the range 30–500 m/s, and fixed for stationary processes. Initial air temperature in melt blowing of polypropylene non-wovens is usually fixed near the level of 300°C.

In the Laval nozzle processes, the pressure of cold (room temperature) air at the nozzle inlet is elevated to the values exceeding a critical value for generation of supersonic air jet and fixed to maintain stationary conditions. The air jet accelerates in the converging entrance of the nozzle to sonic velocity at the nozzle throat, and next continues acceleration to a supersonic level in the diverging part of the nozzle. We consider air-drawing of the polypropylene melt extruded to the supersonic air jet in the single-filament approximation.

In general, pneumatic melt spinning processes are two-phase processes involving polymer streams and the air jets blown along the streams as the phases. In the modeling, dynamic fields of the velocity, temperature, stresses, and/or pressure distributions are considered in each phase. We assume that the dynamic fields of the air, being the working medium in the pneumatic processes, are not affected by the single row of thin polymer filaments and the filaments are considered in thin-, single-filament approximation.[12,13] Experimental investigations indicate negligible influence of single row of the filaments on the dynamic air fields in the pneumatic processes.[14]

In thin-filament approximation, the velocity, temperature, and pressure fields of the air at the filament surface are approximated by the predetermined values along the filament paths at the centerline axis z. Pneumatic melt spinning is driven by air friction forces cumulating along the filament surface and resulting in flow deformation of the melt with the elongational flow dominating over the shear flow. Dominating contribution of the elongational flow results from high aspect ratio of the filament in the process and accumulation of the air friction forces tangential to the filament surface. Radial gradients of the polymer velocity V, temperature T, and components of the stress tensor σ inside the filament are neglected in thin-filament approximation, and the dynamic fields in the polymer bulk are approximated by their average values on the radial filament cross-section, $V(z)$, $T(z)$, $\sigma(z)$.

With the assumptions of longitudinal die assembly and single row of polymer extrusion orifices, modeling of the filament attenuation in both pneumatic processes, melt blowing and Laval nozzle process, separates into two steps. In the first step, predetermined two-dimensional air velocity, temperature, and pressure fields are computed in the cross-section plane normal to the die assembly at the absence of the polymer filament. The second step concerns the dynamics of stationary air-drawing of an individual polymer stream considered with the use of the mathematical model of melt spinning in the single-, thin-filament approximation.

AIR JET FIELDS

The air jet fields in the Laval nozzle process between the polymer extrusion head and the collector are pre-determined based on the mathematical k–ω method.[15–17] High air velocities considered in this process generate high Reynolds numbers in the jet after exiting from the nozzle and the air flow is considered as turbulent.[18] To solve the turbulent phenomena, the average turbulent kinetic energy $k = \langle u_i u_i \rangle/2$ and specific dissipation rate of the kinetic energy $\omega = \varepsilon/k$ are chosen in this model where the average dissipation rate $\varepsilon = \nu\left\langle \frac{\partial u_i}{\partial x_j} \cdot \frac{\partial u_j}{\partial x_i} \right\rangle$, ν is kinematic air viscosity, and Einstein's summation convention is used. Compressible and steady-state two-dimensional air flow is considered in the (y,z) plane normal to the die assembly. It is considered that no air flow in the x-direction along the assembly takes place due to the symmetry. The coordinate system with z-axis identical with the symmetry axis of the nozzle in the cross-section normal to the die assembly is considered. Origin of the z-axis is fixed at the extrusion point of the melt at the center of the orifice exit.

The continuity equation for the two-dimensional air flow with the velocity components U_y, U_z, and the local air density ρ reads

$$\frac{\partial}{\partial y}(\rho U_y) + \frac{\partial}{\partial z}(\rho U_z) = 0. \quad (1)$$

The momentum conservation equations for the z- and y-direction.

$$\rho U_y \frac{\partial U_z}{\partial y} + \rho U_z \frac{\partial U_y}{\partial z} = -\frac{\partial P}{\partial z} + \frac{2}{3}\frac{\partial}{\partial z} \times \left[\rho.(\nu + \nu_T)\left(2\frac{\partial U_z}{\partial z} - \frac{\partial U_y}{\partial y}\right) - \rho k\right] + \frac{\partial}{\partial y}\left[\rho.(\nu + \nu_T)\left(\frac{\partial U_z}{\partial y} + \frac{\partial U_y}{\partial z}\right)\right], \quad (2)$$

$$\rho U_y \frac{\partial U_y}{\partial y} + \rho U_z \frac{\partial U_y}{\partial z} = -\frac{\partial P}{\partial y} + \frac{2}{3}\frac{\partial}{\partial y} \times \left[\rho.(\nu + \nu_T)\left(2\frac{\partial U_y}{\partial y} - \frac{\partial U_z}{\partial z}\right) - \rho k\right] + \frac{\partial}{\partial z}\left[\rho.(\nu + \nu_T)\left(\frac{\partial U_z}{\partial y} + \frac{\partial U_y}{\partial z}\right)\right], \quad (3)$$

where ν, $\nu_T = k/\omega$ are kinematic viscosity and kinematic viscosity of the turbulent motion, respectively, P is air pressure.

The energy conservation equation

$$\rho U_y \frac{\partial H}{\partial y} + \rho U_z \frac{\partial H}{\partial z} = \frac{2}{3}\frac{\partial}{\partial y}\left[\rho.(\nu + \nu_T)U_y\left(2\frac{\partial U_y}{\partial y} - \frac{\partial U_z}{\partial z}\right) - \rho k\right] + \frac{\partial}{\partial y}\left[\rho \cdot (\nu + \nu_T)U_z\left(\frac{\partial U_z}{\partial y} + \frac{\partial U_y}{\partial z}\right)\right] + \frac{\partial}{\partial z}\left[\rho \cdot (\nu + \nu_T)U_y\left(\frac{\partial U_z}{\partial y} + \frac{\partial U_y}{\partial z}\right)\right] + \frac{2}{3}\frac{\partial}{\partial z}\left[\rho(\nu + \nu_T)U_z\left(2.\frac{\partial U_z}{\partial z} - \frac{\partial U_y}{\partial y}\right) - \rho k\right] + \frac{\partial}{\partial y}\left[\rho(\nu + \sigma\nu_T)\frac{\partial k}{\partial y}\right] + \frac{\partial}{\partial z}\left[\rho(\nu + \sigma\nu_T)\frac{\partial k}{\partial z}\right] + \frac{\partial}{\partial y}\left[\rho\left(\frac{\nu}{\mathrm{Pr}_L} + \frac{\nu_T}{\mathrm{Pr}_T}\right)\frac{\partial}{\partial y}\left(c_v T_a + \frac{P}{\rho}\right)\right] + \frac{\partial}{\partial z}\left[\rho\left(\frac{\nu}{\mathrm{Pr}_L} + \frac{\nu_T}{\mathrm{Pr}_T}\right)\frac{\partial}{\partial z}\left(c_v T_a + \frac{P}{\rho}\right)\right], \quad (4)$$

where $H = c_V T_a + \frac{P}{\rho} + k + \frac{1}{2}\left(U_y^2 + U_z^2\right)$ is total enthalpy, c_V is specific heat of the air at constant volume, T_a is absolute air temperature, and Pr_L, Pr_T is laminar and turbulent Prandtl numbers.

The equations of turbulent kinetic energy k and specific dissipation rate ω read

$$\rho U_y \frac{\partial k}{\partial y} + \rho U_z \frac{\partial k}{\partial z} = \frac{2}{3}\left[\rho.\nu_T\left(2\frac{\partial U_y}{\partial y} - \frac{\partial U_z}{\partial z}\right) - \rho k\right] \times \frac{\partial U_y}{\partial y} + \rho\nu_T\left(\frac{\partial U_z}{\partial y} + \frac{\partial U_y}{\partial z}\right)^2 + \frac{2}{3}\left[\rho.\nu_T\left(2\frac{\partial U_z}{\partial z} - \frac{\partial U_y}{\partial y}\right) - \rho k\right] \times \frac{\partial U_z}{\partial z} - \beta^*\rho\omega k + \frac{\partial}{\partial y}\left[\rho(\nu + \sigma^*\nu_T)\frac{\partial k}{\partial y}\right] + \frac{\partial}{\partial y}\left[\rho(\nu + \sigma^*\nu_T)\frac{\partial k}{\partial y}\right], \quad (5)$$

$$\rho U_y \frac{\partial \omega}{\partial y} + \rho U_z \frac{\partial \omega}{\partial z} = \frac{4}{3}\gamma\frac{\omega}{k}\rho\nu_T\left[\left(\frac{\partial U_y}{\partial y} - \frac{\partial U_z}{\partial z}\right)^2 + \frac{\partial U_z}{\partial z}\cdot\frac{\partial U}{\partial y}\right] - \beta\rho\omega^2 + \frac{\partial}{\partial y}\left[\rho(\nu + \sigma\cdot\nu_T)\frac{\partial \omega}{\partial y}\right] + \frac{\partial}{\partial y}\left[\rho(\nu + \sigma.\nu_T)\frac{\partial \omega}{\partial z}\right] \quad (6)$$

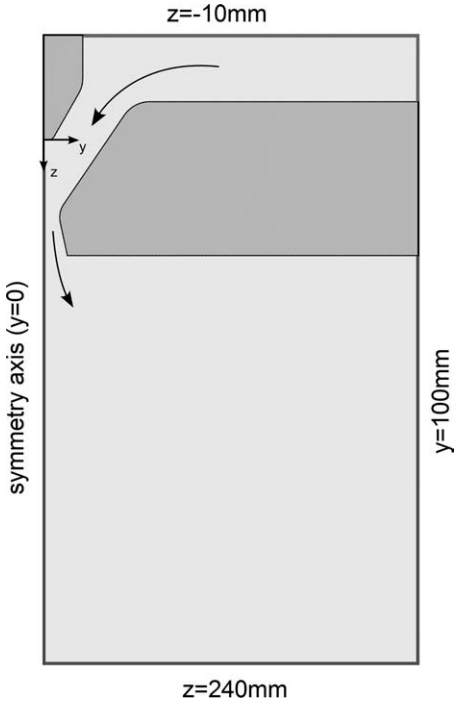

Figure 2 Geometry of the Laval nozzle and the air jet computational domain with the symmetry axis $y = 0$.

where $\gamma = 0.8$, $\beta = 0.075$, $\sigma = 0.5$, $\beta^* = 0.09$, $\sigma^* = 0.5$. The equation of state of ideal gas is applied, $P = \rho R T_a$, where R is the gas constant.

Due to symmetry of the flow fields, the numerical domain in the simulations reduces to the half of the two-dimensional field, with the symmetry axis of the fields at the edge. For the Laval nozzle geometry and the computational domain presented in Figure 2, the boundary conditions for the equations read:

-inlet to the nozzle, $z = -10$ mm: $P = P_{\mathrm{amb}} + \Delta P$, $k = \omega = 0$, $T_a = T_0$,
-the wall of nozzle: $U_y = U_z = k = \omega = 0$, $T_a = T_{\mathrm{amb}}$,
-the symmetry axis $y = 0$: $\frac{\partial U_z}{\partial y} = \frac{\partial T_a}{\partial y} = \frac{\partial P}{\partial y} = \frac{\partial k}{\partial y} = \frac{\partial \omega}{\partial y} = 0$, $U_y = 0$,
-outlet of the domain, $z = 240$ mm and $y = 100$ mm: $\frac{\partial k}{\partial y} = \frac{\partial \omega}{\partial z} = 0$

where ΔP is air compression at the nozzle inlet, T_{amb} and P_{amb} is ambient temperature and pressure.

The air fields has been computed based on the eqs. (1)–(6), the state equation of ideal gas, and the boundary conditions using the finite volume elements method of the computational fluid dynamics and the Fluent 12 package. Several mesh resolution tests were performed to evaluate the grid convergence index (GCI)[19] and to identify the optimal mesh resolution, being compromise of the computational time and the numerical accuracy. The most critical flow region of the domain is located within

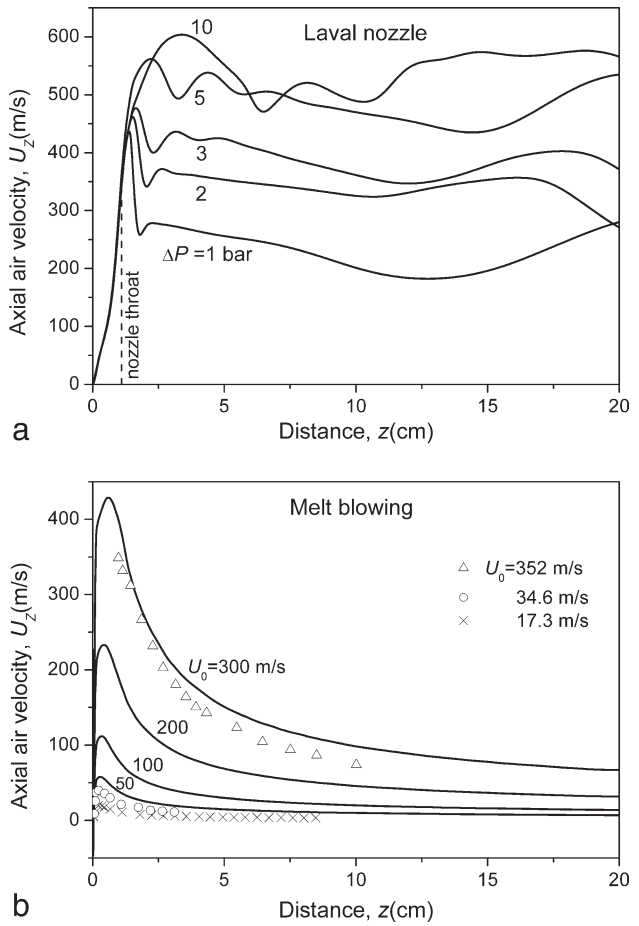

Figure 3 Axial air velocity profiles versus distance z computed for: (a) Laval nozzle process with room temperature air at the nozzle inlet and air compressions ΔP, (b) melt blowing with the initial air temperature 300°C and initial air velocities U_0 (lines[20]) and the experimental data.[22,23]

the narrowing of the Laval nozzle. Based on the test simulations in this region, the optimal mesh sought using GCI was found for the model to consist of 143,795 grid cells, with the distance between grid nodes of about 0.4 mm and the error of the computations <1%.

The computations of the air fields have been performed for the inlet air temperature of 20°C and several air compression values ΔP at the nozzle inlet between 1 and 10 bars. Figures 3(a) and 4(a) present the computed air velocity and temperature distributions along the symmetry axis z of the jet, since this region controls dynamics of air-drawing of the filament. For comparison, axial distributions of the air velocity and temperature computed for melt blowing at several initial air velocities U_0 in the range 50–300 m/s in a separate publication[20] with the aid of the Fluent package are presented in Figures 3(b) and 4(b) (line plots). The computations were performed for the initial air temperature fixed to 300°C using the k–ε model of turbulent flow which consists of a system of differential equations in the (y,z) plane for the mass continuity, momentum and energy conservation, turbulent kinetic energy k, the turbulent dissipation rate ε, and the state equation of ideal gas.[15,20,21] The die assembly with the blunt nose recessed by 0.3 mm, the width of the slots of 0.5 mm, the air slots inclination angle 28.25° to the z-axis was assumed in that computations. Zero of the z-axis is fixed at the exit of the polymer extrusion orifice.

The experimental points presented in Figures 3(b) and 4(b) provide satisfactory verification of the simulation results obtained for melt blowing and confirm general character of the computed axial profiles of air velocity and temperature, as well as the influence of the initial air velocity on the profiles. In the vicinity of the air slots, the axial air velocity rapidly increases to a maximum within a few millimeters. The maximum is followed by a monotonic decay of the air velocity along the z-axis. Such a decaying character show also axial profiles of the air temperature.

No experimental data are available in the literature for verification of the air fields simulated for

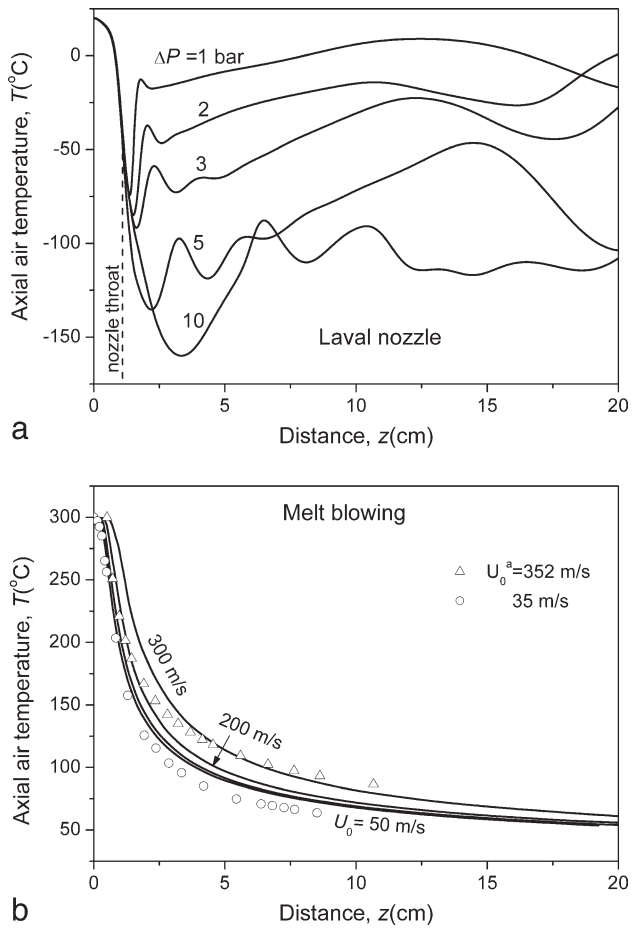

Figure 4 Axial air temperature profiles versus distance z computed for: (a), (b) as in Figures 3(a,b).

the supersonic Laval nozzle processes. Validation of the computations performed for the supersonic air jets bases on the numerical criteria of convergence at the mesh resolution and the number of computation cycles adjustment. The air velocity and temperature profiles presented in Figures 3(a,b) and 4(a,b) illustrate fundamental differences in the dynamics of the air jets in the Laval nozzle and melt blowing processes. In the Laval nozzle process, the air accelerates rapidly in the convergent inlet of the nozzle to the velocity of sound at the nozzle throat point. In the divergent outlet of the nozzle, the velocity increases further to supersonic values and remains at high level over a considerable range of the axis without decaying. The computed Mach number achieves the values between unity and three in the nozzle range, depending upon the air compression at the inlet. Behind the nozzle, the Mach number decreases but it is still relatively high.

The air temperature is predicted to decrease along the z-axis for every air compression value at the nozzle inlet, from room temperature at the inlet to a minimum in the diverging part of the nozzle where the air decompresses. Next, the air temperature increases after the nozzle exit, with some waving, to values still remaining much below the ambient room temperature. The computed air pressure (not shown in the figures) rapidly drops down to the ambient value at the nozzle outlet and remains at this level in the whole area outside the nozzle. The air decompression in the nozzle is accompanied by rapid decrease in the air temperature. In melt blowing, the simulated air pressure shows a slight increase within a few millimeters of the jet axis followed by rapid decay to the ambient value. The axial distributions of the air velocity, temperature, and pressure obtained for the Laval nozzle air jet are used in the computations of the dynamic profiles of air-drawing of the polymer melt in the Laval nozzle process, for comparison with the dynamics of melt blowing.

DYNAMICS OF AIR-DRAWING

Air-drawing of the polymer filament and its attenuation in the pneumatic processes take place within the range of the process axis where the air velocity exceeds velocity of the polymer. The supersonic Laval nozzle process differs from melt blowing by application of cold air and much higher air velocity, non-decaying over a significant range of the process axis. Such an air jet allows air-drawing of the polymer filament over a much longer range of the axis without coiling. To discuss dynamics of air-drawing in both pneumatic processes, mathematical model of stationary fiber melt spinning in single-, thin-filament approximation is applied.[24,25] Relatively low volume concentration of the filaments in the spinning space allows to neglect inter-filament aerodynamic interactions. In the model, attenuation of an individual thin polymer stream extruded along the symmetry axis of the planar air fields from a circular cross-section orifice is considered. Dynamics of air-drawing of the filament is calculated using the predetermined axial distribution of the air fields.

The model of melt air-drawing consists of a set of first order ordinary differential equations for the local polymer velocity $V(z)$, temperature $T(z)$, tensile stress $\Delta p(z)$, and rheological extra-pressure $p_{\mathrm{rh}}(z)$. The equations result from the mass, force, energy conservation equations, and the constitutive equation of viscoelasticity. Preliminary computations performed for air-drawing of isotactic polypropylene (iPP) in the Laval nozzle process indicate no online crystallization of the polymer because temperature of the polymer does not fall below the critical temperature of crystallization enough early before reaching the collector, similarly as it was predicted for melt blowing of iPP.[13,26]

The mass conservation equation of stationary polymer stream

$$\frac{\pi D^2(z)}{4}\rho(z)V(z) = W = \mathrm{const} \tag{7}$$

provides relation between the polymer velocity $V(z)$ and local filament diameter $D(z)$, valid in the range of z-axis where the air velocity is higher than the velocity of the filament, $U(z) > V(z)$. The temperature dependence of the polypropylene melt density reads[27]

$$\rho_a[T(z)] = \frac{10^3}{1.145 + 9.03 \times 10^{-4}[T(z) - 273]}\,(\mathrm{in\ kg/m^3}) \tag{8}$$

where $T(z)$ is the polymer absolute temperature.

The axial gradient of the tensile force $F(z)$ results from the force balance equation of the filament and accounts for the inertia, air friction, and gravity forces, respectively.

$$\frac{dF}{dz} = W\frac{dV}{dz} + \frac{dF_a}{dz} - \frac{\pi D^2(z)}{4}\rho(z)g. \tag{9}$$

Axial gradient of the air friction forces

$$\frac{dF_a}{dz} = -\frac{\pi D(z)}{2}\rho_a(z)C_f(z)[U(z) - V(z)]^2 \tag{10}$$

is negative in the air-drawing range and depends on the difference of the air and the filament axial velocities, $U(z)-V(z)$. The air friction coefficient $C_f(z)$ is assumed with the numerical parameters for the

turbulent boundary layer suggested for pneumatic processes by Majumdar and Shambaugh[28]

$$C_f(z) = 0.78\left[\frac{D(z)|U(z) - V(z)|}{\nu_a(z)}\right]^{-0.61}. \quad (11)$$

Local air density $\rho_a(z) = \text{const}\ P(z)/T_a(z)$ depends on the air pressure and temperature along the z-axis and is determined for dry air assuming $\rho_a(z) = 352.32/T_a(z)$ (in kg/m^3) for the air under atmospheric pressure. Local kinematic viscosity of dry air under pressure P_a reads[25]

$$\nu_a(z) = 4.1618 \times 10^{-9}\frac{T_a^{5/2}(z)}{T_a(z) + 114}\frac{P_{\text{amb}}}{P_a(z)}\ \text{(in m}^2\text{/s)}. \quad (12)$$

The air friction on the filament surface provides driving force of pneumatic melt spinning processes, with negative gradient of the air friction forces in the air-drawing range, $U(z) - V(z) > 0$, which cumulates the tensile force nearby the extrusion point. The cumulated tensile force leads to sharp attenuation of the filament diameter observed in the range of a few centimeters next to the spinneret and fast increase of the filament elongation rate in the pneumatic processes.[29]

Axial gradient of the filament temperature, dT/dz, expresses by the equation

$$\rho(z)C_p(z)V(z)\frac{dT}{dz} = -\frac{4\alpha^*(z)}{D(z)}[T(z) - T_a(z)] + \frac{4F(z)}{\pi D^2(z)}\frac{dV}{dz} \quad (13)$$

which accounts for convective heat exchange between the filament and the air dependent on the local difference of the filament and air temperatures, $T(z) - T_a(z)$, as well as for viscous friction heat generated in the polymer bulk under high-velocity gradient, dV/dz.[13] $C_p(z)$ is the specific heat of the melt dependent on its local temperature.

$$C_p(z) = C_{p0} + C_{p1}[T(z) - 273] \quad (14)$$

with $C_{p0} = 1.5358\times10^3$ J/(kg·K), $C_{p1} = 10.13$ J/(kg·K^2) for polypropylene.[27] The convective heat exchange coefficient $\alpha^*(z)$ determined from the correlation between the Nusselt and Reynolds numbers, $\text{Nu} = 0.42\ \text{Re}^{1/3}$, and confirmed for melt blowing of polypropylene by Bansal and Shambaugh[29] is used.

$$\alpha^*(z) = \frac{0.42\lambda_a(z)}{D(z)^{2/3}}\left[\frac{|U(z) - V(z)|}{\nu_a(z)}\right]^{1/3}. \quad (15)$$

The air fields computed for the Laval nozzle and melt blowing[20] processes indicate that the air flow is coaxial with the jet's centerline and normal component of the air velocity vanishes. Sutherland formula is used for the temperature dependence of the air conductivity coefficient.[25]

$$\lambda_a(z) = 2.0848 \times 10^{-3}\frac{T_a^{3/2}(z)}{T_a(z) + 114}\ \text{(in J/(m} \cdot \text{s} \cdot \text{K))}. \quad (16)$$

For uniaxial elongational flow of the polymer melt, the axial and radial stress components, p_{zz}, p_{rr}, determine tensile stress $\Delta p = p_{zz} - p_{\text{rr}}$ and the rheological pressure $p = -(p_{zz} + 2p_{\text{rr}})/3$. The local stress tensor $\mathbf{p}(z)$ in the polymer bulk expresses by the local air pressure $P(z)$ and the extra-stress tensor $\sigma(z)$, $\mathbf{p}(z) = -P(z)\mathbf{I} + \sigma(z)$, where $\mathbf{I}$ is a unit tensor. In steady-state air-drawing of the melt and thin-filament approximation, the local tensile stress $\Delta p(z)$ is associated with the local tensile force $F(z)$ acting on the filament cross-section

$$\Delta p(z) = p_{zz} - p_{rr} = \sigma_{zz}(z) - \sigma_{rr}(z) = \frac{4F(z)}{\pi D^2(z)}. \quad (17)$$

The local pressure in the filament

$$p(z) = -\frac{1}{3}(p_{zz} + 2p_{rr}) = P(z) - \frac{1}{3}(\sigma_{zz} + 2\sigma_{rr}) \quad (18)$$

where the second term is the rheological extra-pressure determined by the extra-stress components.

$$p_{\text{rh}}(z) = -\frac{1}{3}(\sigma_{zz} + 2\sigma_{rr}). \quad (19)$$

Phan-Thien/Tanner constitutive equation of nonlinear viscoelasticity[30,31] is used to determine the tensile stress and rheological extra-pressure. The following differential equations are obtained[12] for the tensile stress, $\Delta p(z)$, and rheological extra-pressure, $p_{\text{rh}}(z)$, for steady-state uniaxial air-drawing of the polymer melt in thin-filament approximation.

$$\tau(z)V(z)\frac{d}{dz}\Delta p + \Delta p(z)\exp\left[-3 \in \frac{\tau(z)}{\eta(z)}p_{\text{rh}(z)}\right] = 3\eta(z)\frac{dV}{dz} + \tau(z)(1 - \xi)[\Delta p - 3p_{\text{rh}}(z)]\frac{dV}{dz} \quad (20)$$

$$\tau(z)V(z)\frac{d}{dz}p_{\text{rh}} + p_{\text{rh}}(z)\exp\left[-3 \in \frac{\tau(z)}{\eta(z)}p_{\text{rh}}(z)\right] = -\frac{2}{3}\tau(z)(1 - \xi)\Delta p(z)\frac{dV}{dz} \quad (21)$$

where $\eta(z)$ is local Newtonian viscosity, $\tau(z)$ is relaxation time dependent on local temperature $T(z)$. The parameters $\in = 0.015$ and $\xi = 0.6$ responsible for

non-linear elasticity and shear thinning effects are assumed for iPP melt.[32]

The temperature dependence of the Newtonian viscosity of the amorphous polymer is assumed in the Arrhenius form, with the front factor η_0 dependent on the weight-average molecular weight M_w.

$$\eta(T) = \begin{cases} \eta_0(M_w)\exp\left(\frac{E_D}{kT}\right) & T > T_g \\ \infty & T \le T_g \end{cases} \quad (22)$$

where E_D is activation energy of viscous motion, T_g is glass transition temperature, k is the Boltzmann constant, $\eta_0(M_w) = \text{Const} \cdot M_w^{3,4}$.[33] For iPP, we have $E_D/k = 5292\text{K}$ and $T_g = 253\text{K}$.[24,34] With a reference shear viscosity η_{ref} at a reference molecular weight $M_{w,\text{ref}}$ and temperature T_{ref} we have

$$\eta_0(M_w) = \eta_{\text{ref}}(T_{\text{ref}}; M_{w,\text{ref}})\left(\frac{M_w}{M_{w,\text{ref}}}\right)^{3.4} \exp\left(-\frac{E_D}{kT_{\text{ref}}}\right). \quad (23)$$

$\eta_{\text{ref}} = 3000$ Pa s is chosen as the reference viscosity of iPP melt at 220°C and $M_{w,\text{ref}} = 300{,}000$.[33]

The relaxation time $\tau(z)$ of the melt is determined from the ratio $\tau(z) = \eta(z)/G(z)$ of shear viscosity and the modulus of elasticity proportional to the local polymer temperature, $G(z) = BT(z)$. The constant $B = k(1 - \xi)^2\mu$ is proportional to the volume concentration of sub-chains between the entanglements, μ, independent of the polymer molecular weight[31], and the molecular weight dependence of $\tau(z)$ results from the melt viscosity.

For local modulus of elasticity of the melt at $T(z)$ expressed by a reference modulus at T_{ref}, $G(z) = G_{\text{ref}}(T_{\text{ref}})T(z)/T_{\text{ref}}$, the relaxation time $\tau(z)$ reads,

$$\tau(z) = \tau_{\text{ref}}\left(\frac{M_w}{M_{w,\text{ref}}}\right)^{3.4} \exp\left[\frac{E_D}{k}\left(\frac{1}{T(z)} - \frac{1}{T_{\text{ref}}}\right)\right]\frac{T_{\text{ref}}}{T_z} \quad (24)$$

where $\tau_{\text{ref}} = \eta_{\text{ref}}(T_{\text{ref}}, M_{w,\text{ref}})/G_{\text{ref}}(T_{\text{ref}})$ is a reference relaxation time of the polymer melt at the reference temperature and reference molecular weight. The reference relaxation time 0.035 s is used, estimated for 220°C and $M_{w,\text{ref}} = 300{,}000$ from the relaxation time of 0.040 s reported for the iPP grade of shear viscosity 3420 Pa·s at 210°C.[32]

The mathematic model of melt air-drawing presented by eqs. (7,9,13,17,20,21) leads to four ordinary differential equations of first order for the axial profiles $V(z)$, $T(z)$, $F(z)$, and $p_{\text{rh}}(z)$. Runge-Kutta numerical integration procedure has been used to compute the profiles with the stationary conditions for initial melt velocity $V(z = 0) = V_0 = 4W/[\pi D_0^2 \rho(T_0)]$, temperature $T(z = 0) = T_0$, and the rheological extra-pressure p_{rh} $(z = 0) = 0$ at the melt extrusion point, $z = 0$, from a circular orifice of a diameter D_0. The initial condition for the tensile force, $F(z = 0) = F_0$, is adjusted by an inverse method to the zero tensile force at the free end of the filament deposited onto the collector, $F(z = L) = 0$, in the non-wovens formation processes.

RESULTS AND DISCUSSION

In the computations for air-drawing of iPP melt in the Laval nozzle process we assume initial temperature 300°C of the polymer at the extrusion point. It is reported in the literature[6] that the diameter D_0 of the extrusion orifices in the Laval nozzle processes is larger by a factor of 2–3 than that used in melt blowing. This leads to higher mass outputs W of the polymer melt by a factor of 4–9, respectively, at the same polymer extrusion velocity. We assume $D_0 = 0.7$ mm and $W = 0.04$ g/s per single orifice for the Laval nozzle process. At these values, the initial melt velocity V_0 in the Laval nozzle process is the same as in the computations performed for melt blowing with $D_0 = 0.35$ mm and $W = 0.01$ g/s.[13]

Figure 5(a) show profiles of the iPP filament velocity $V(z)$ between the extrusion point $z = 0$ and the collector located at $z = 20$ cm (solid lines), obtained from the computations for the Laval nozzle process and different values of the melt extrusion viscosity at 300°C. The viscosities are in the range 64–671 Pa s and corresponds to the melt flow rate index in the range 65–6 [g/10 min], calculated from the formula MFR = Const/η(230°C) at Const = 15,000 Pa·s,[33] and to molecular weight M_w between 150,000 and 300,000 with a step of 50,000, respectively. The computations have been performed from the model equations for air-drawing of the melt by the supersonic air jet with the air velocity distribution (dashed line) obtained for the air compression of two bars in the nozzle inlet. In this process, air velocity dominates along the entire processing axis over the filament velocity predicted for each melt extrusion viscosity, and the polymer is subjected to air-drawing between the extrusion point and the collector.

The filament velocity increases along the process axis to the highest values at the collector, which are higher for lower melt viscosities. For the extrusion viscosity of 169 Pa s (MFR = 24), the filament velocity is predicted to be as high as 10,000 m/min at the collector. At 64 Pa s (MFR = 65), the filament velocity profile discontinues before the collector due to an instability which results from a divergence of the filament velocity in the computations. The divergence may indicate a failure of the steady-state model of air-drawing for the lower polymer extrusion viscosities.

For comparison with the Laval nozzle process, Figure 5(b) illustrates filament velocity distribution

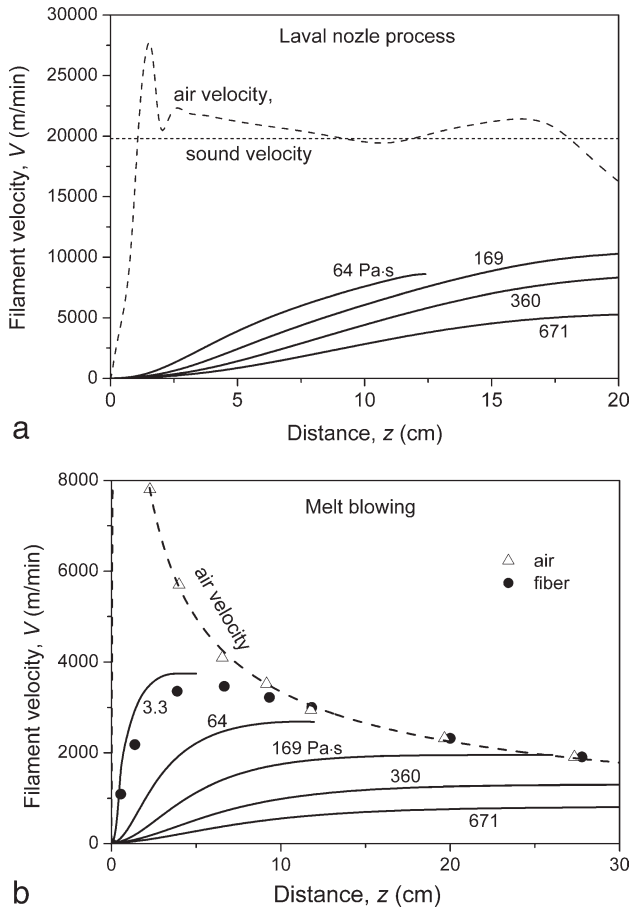

Figure 5 Filament velocity versus distance z computed for several extrusion viscosities of the iPP melt (solid lines). (a) Laval nozzle process with the air velocity distribution computed for $\Delta P = 2$ bars (dashed line); (b) melt blowing with the air velocity distribution (dashed line) adjusted to experimental data[1] (open symbols) with initial air temperature 300°C, solid symbols—filament velocity experimental data[1] for MFR = 1259 (melt extrusion viscosity of 3.3 Pa s at 300°C).

in melt blowing (solid lines) computed for the same values of the melt extrusion viscosity at 300°C, the same collector location at $z = 20$ cm, and the air velocity distribution (dashed line) fitting to the experimental data (points).[1] The decaying air jet in melt blowing causes that the range of air-drawing is limited at lower extrusion viscosities by the point where the air velocity approaches velocity of the filament. Such a character of the air jet is confirmed by experimental data[1] presented in Figure 5(b) which show limited range of the process axis where the air velocity exceeds velocity of the filament. The air-drawing zone extends from the melt extrusion point to the position on the z-axis at which both velocities coincide. Extent of the air-drawing zone in melt blowing is determined by the decaying character of the air jet and by the dynamics of the filament air-drawing. Beyond that zone the filaments decelerate and undergo intensive coiling observed in the experiments before achieving the collector.[1] The transition from the air-drawing to the deceleration & coiling zone takes place in the range of the process axis where the maximum of the filament velocity is seen in the experimental data. The computations indicate that the coiling zone appears earlier on the z-axis for lower melt extrusion viscosities, at which higher velocity and stronger attenuation of the filament is predicted.

Figures 6(a)–9(a) illustrate influence of the air jet velocity on the filament velocity, diameter, temperature, and tensile stress in the Laval nozzle process predicted for several values of the air compression ΔP from the range 1–10 bars, fixed melt extrusion viscosity of 360 Pa s (MFR = 12) in the nozzle inlet, and the collector distance of 20 cm from the extrusion point. For comparison, Figures 6(b)–9(b) show the profiles computed for melt blowing for several values of the initial air velocity from the range 50–300 m/s, at the same collector position $z = 20$ cm and melt extrusion viscosity of 360 Pa s.

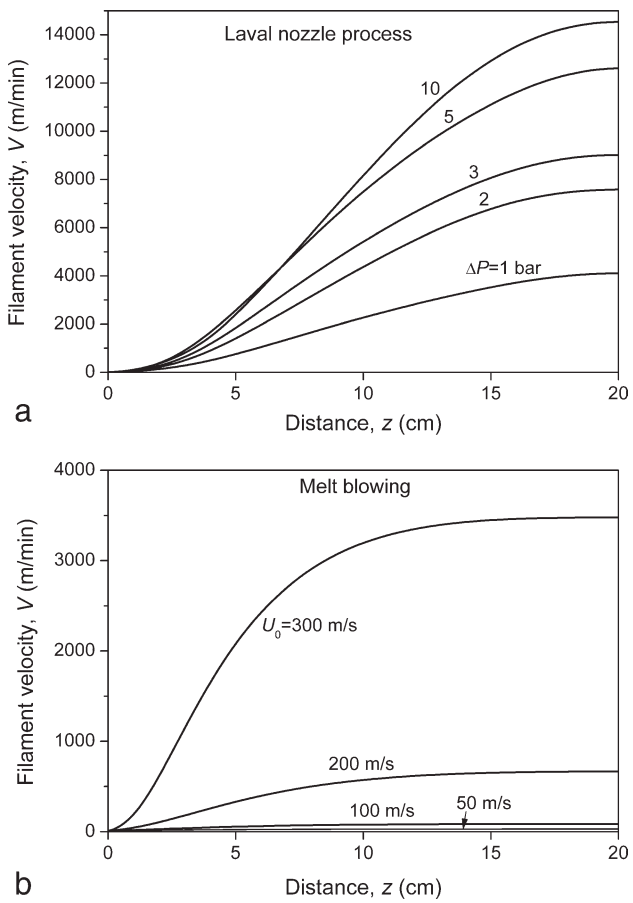

Figure 6 Filament velocity V versus distance z computed for iPP. (a) Laval nozzle process for several ΔP values; (b) melt blowing for several U_0 values and $T_0 = 300$°C. Melt extrusion viscosity of 360 Pa s at 300°C (MFR = 12) and the collector located at $z = 20$ cm.

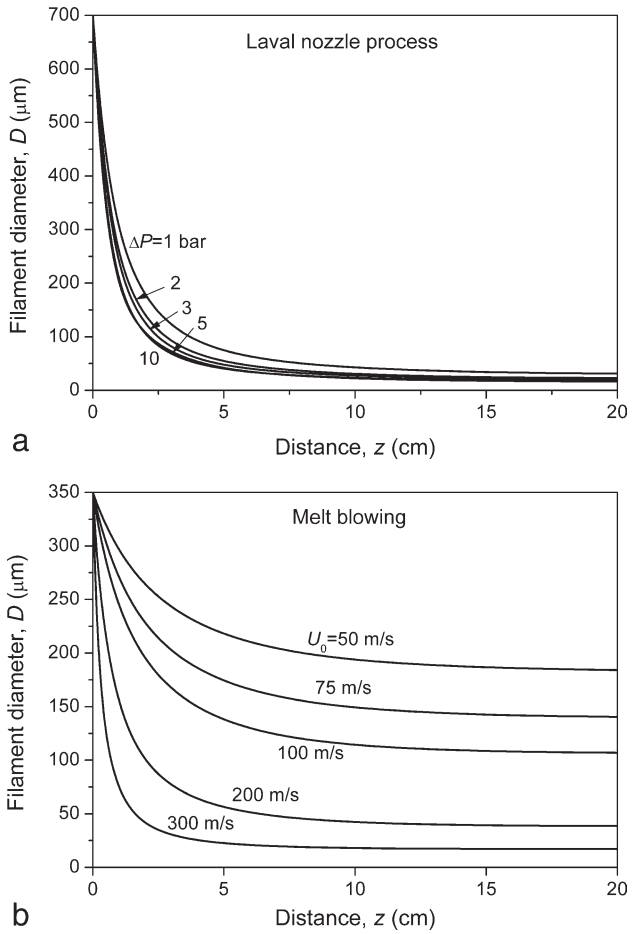

Figure 7 Filament diameter D versus distance z computed for iPP. (a) Laval nozzle process for several ΔP values; (b) melt blowing for several U_0 values and T_0 = 300°C. Melt extrusion viscosity of 360 Pa s at 300°C (MFR = 12) and the collector located at z = 20 cm.

The filament velocity predicted for the highest initial air velocity in melt blowing [Fig. 6(b)] approaches at the collector the values known from high-speed melt spinning. But the values in melt blowing are achieved within much shorter range of the process axis due to much higher elongation rate predicted for about 300 s^{-1} at its maximum. In the Laval nozzle process, under the supersonic air jet computed for ΔP = 2 bars, the filament velocity at the collector [Fig. 6(a)] achieves twice higher level than in high-speed melt spinning and the melt elongation rate is as high as 1000 s^{-1} at the maximum. Higher air compressions in the Laval nozzle inlet lead to higher elongation rates, higher filament velocities, and attenuation.

Majority of the filament diameter attenuation in both pneumatic processes is predicted to takes place next to the extrusion point within the range of 4–5 cm [Fig. 7(a,b)]. In melt blowing, the attenuation is very sensitive to the initial air velocity, from a relatively weak at low initial air velocities to very high for the fastest air jets. For the Laval nozzle process, attenuation of the filament diameter is predicted to be similar for each air compression leading to supersonic air jet and very high.

The predicted filament temperature versus distance z remains above the equilibrium melting point T_m^0 of iPP in both pneumatic processes [Fig. 8(a,b)] and the polymer should not crystallize online before achieving the collector. In the computations, temperature of the filament approaching the collector is close to $T_m{}^0$, with a deviation not exceeding 30°C. Influence of the air compression in the Laval nozzle inlet, or of the initial air velocity in melt blowing, on the axial profile of the filament temperature is not significant in both pneumatic processes, but with the opposite effects. In the Laval nozzle process at higher ΔP, the filament temperature predicted at the collector is in general lower, while at higher initial air velocities U_0 in melt blowing it is higher.

The air temperature predicted for the supersonic Laval nozzle process remains at a level of −50°C

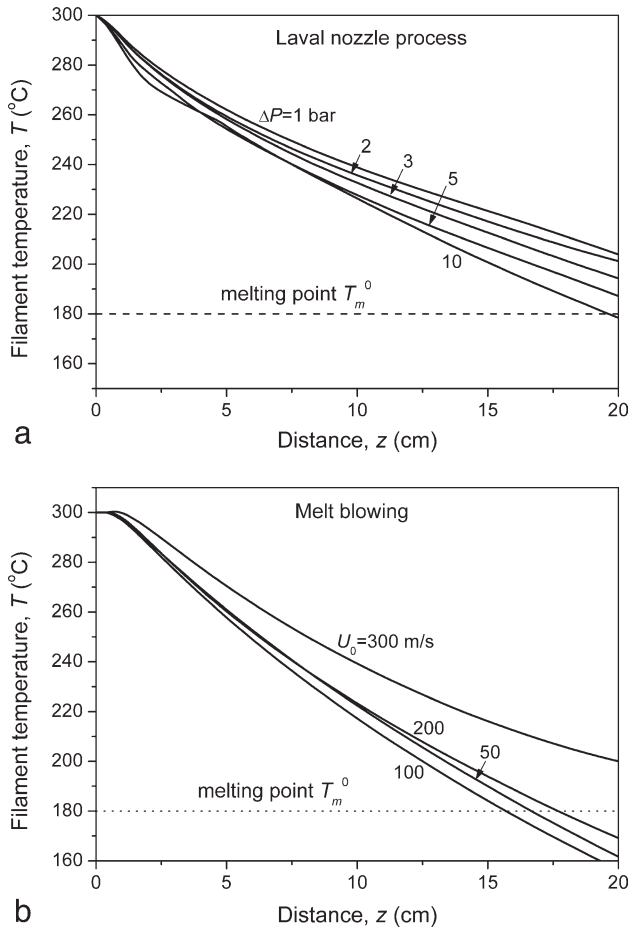

Figure 8 Filament temperature T versus distance z computed for iPP. (a) Laval nozzle process for several ΔP values; (b) melt blowing for several U_0 values and T_0 = 300°C. Melt extrusion viscosity of 360 Pa s at 300°C (MFR = 12) and the collector located at z = 20 cm.

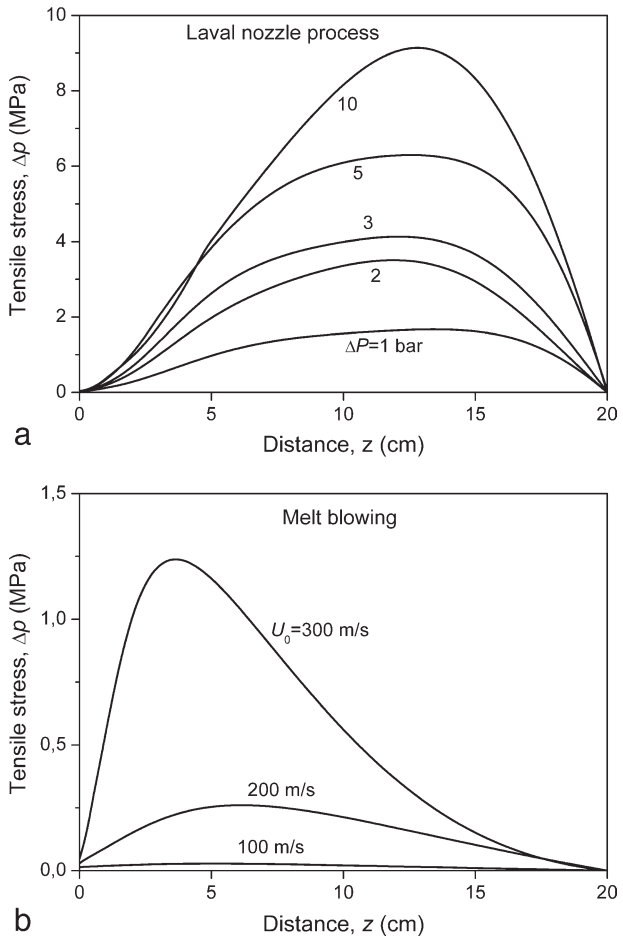

Figure 9 Tensile stress Δp versus distance z computed for iPP. (a) Laval nozzle process for several ΔP values; (b) melt blowing for several U_0 values and $T_0 = 300$°C. Melt extrusion viscosity of 360 Pa s at 300°C (MFR = 12) and the collector located at $z = 20$ cm.

down to −100°C along the majority of the process axis, depending upon the inlet air compression ΔP, while in melt blowing it is higher by the order of 100–200°C [Fig. 4(a,b)]. It is surprising that temperature of the filaments computed for the supersonic processes at various ΔP values remains generally higher along the axis than in melt blowing despite much lower air temperature in the supersonic process and does not fall below $T_m{}^0$ [Fig. 8(a,b)]. This is an effect of higher mass output of the polymer melt, $W = 0.04$ g/s per orifice, assumed in this computations for the Laval nozzle process versus $W = 0.01$ g/s per orifice assumed for melt blowing. In these computations, the orifice diameter is twice higher in the Laval nozzle process to preserve the same value of the melt extrusion velocity in both pneumatic processes. In the literature, the Laval nozzle processes are characterized by the mass outputs several times higher than in melt blowing, with the diameter of the melt extrusion orifice twice higher or more.[6]

Higher mass output W reduces contribution of the convective heat exchange between the filament and the air, $-\beta_{con}(z)[T(z) - T_a(z)]$, to the axial gradient of the filament temperature dT/dz where,

$$\beta_{con}(z) = -\frac{0.42\pi\lambda_a(z)}{WC_p(z)}\left[\frac{D(z)|U(z) - V(z)|}{\nu_a(z)}\right]^{1/3} \quad (25)$$

is a coefficient which represents intensity of axial cooling by the convective heat exchange per one degree of the difference in the polymer and air temperatures at the point z. In melt bowing, the computed values of $\beta_{con}(z)$ vary from about 9–10 m^{-1} near the extrusion point for all initial air velocities U_0 considered to nearly fixed value of about 5 m^{-1} in the range of the process axis from the middle ($z = 10$ cm), down to the collector ($z = 20$ cm) for $U_0 = 100$ m/s. For $U_0 = 200$ m/s and 300 m/s, the $\beta_{con}(z)$ values in the middle are of about 4.3 m^{-1} and 3.3 m^{-1}, respectively, and next they continuously diminish to about 2.1 m^{-1} for both initial air velocities at approaching the collector. Values of $\beta_{con}(z)$ obtained in the computations for the Laval nozzle process vary from about 3 m^{-1} near the extrusion point down to nearly fixed values of about 1.6 m^{-1} at the middle and the rest of the process axis for all of the air compressions ΔP considered.

The computations indicate about three times lower axial cooling intensity near the melt extrusion point (per one degree of the difference in the filament and air temperatures) in the Laval nozzle process than in melt blowing, about 3–2 times lower in the middle and about 3–1.3 lower at the end of the process axis, depending upon the initial air velocity U_0. This provides an explanation for the axial distributions of the filament temperature predicted for the Laval nozzle processes on the level comparable with those predicted for melt blowing, despite 2–3 times higher differences in the filament and air temperatures in the Laval nozzle processes. This is a consequence of the mass output W considered in the Laval nozzle process four times higher than in melt blowing, which reduces coefficient $\beta_{con}(z)$ by a factor of 4. Smaller reduction of the coefficient than expected from the W value results from higher differences between the filament and air velocities in the Laval nozzle processes than in melt blowing [eq. (25)].

Local cooling rate of the polymer via the convective heat exchange, $dT/dt = -\beta_{con}(z)[T(z) - T_a(z)]V(z)$, estimated in the computations for the Laval nozzle processes for $\Delta P = 1$, 3, and 5 bars is of about 1.4×10^4, 4.0×10^4, and 6.2×10^4°C/s in the middle of the process axis ($z = 10$ cm), respectively, and further increase of the cooling rate by about 40% at the ultimate part of the axis is predicted. In melt blowing, the estimated values of the cooling rate are of about 1.0×10^3, 6.2×10^3, and 2.8×10^4°C/s for the initial air velocities $U_0 = 100$, 200, and 300 m/s, respectively. Higher cooling rates of the polymer, dT/dt, at

higher filament velocities $V(z)$ in the Laval nozzle processes result in axial gradients of the filament temperature dT/dz similar to those obtained in the computations for melt blowing, as well as in similar axial temperature profiles remaining generally above $T_m{}^0$ in both pneumatic processes. Such a feature of melt cooling along the process axis in the Laval nozzle process allows for melt bonding of the non-wovens during cooling on the collector, similarly as in melt blowing with the application of hot air.

Total contribution of the viscous friction heat generated in the polymer bulk under high-velocity gradient dV/dz in eq. (13) elevates the predicted filament temperature by about 1.2, 3.6, and 4.7°C at the end of the process axis in the Laval nozzle case for the discussed air compressions, respectively, and is much lower than the contribution of the convective heat exchange. In melt blowing, the viscous friction generates lower elevation of the polymer temperature, by 1.1°C at the end of the process axis for the initial air velocity $U_0 = 300$ m/s and lower for lower U_0 values.

Axial profiles of the tensile stresses presented in Figures 9(a,b) for both pneumatic processes indicate tensile stresses higher by an order of magnitude for the Laval nozzle process, with a maximum of the stress at a higher distance from the extrusion point. The tensile stress increases significantly with ΔP. It predicts higher stream birefringence in the supersonic Laval nozzle process than in melt blowing. In melt blowing, maximum of the tensile stress locates closer to the extrusion point, in the range where majority of the filament attenuation is predicted. In both processes, the tensile stress vanishes at the free end of the filament on the non-woven surface. Nevertheless, the tensile stress vanishes rather abruptly in the Laval nozzle case because the stress remains at much higher level over wider range of the processing axis due to non-decaying character of the air jet in this range, in comparison with decaying air jet in melt blowing [Fig. 3(a,b)]. One could expect that the tensile stress in the Laval nozzle process should vanish more softly at higher distances from the extrusion point, but at higher distances between die and the collector.

Negative rheological extra-pressure is predicted to be created inside the iPP filament at fast elongation under supersonic jets in Laval nozzle process. The negative pressure appears inside the Laval nozzle throat in a narrow range of about 20–25 mm of the air-drawing axis, next to the extrusion point. Maximum of the absolute extra-pressure value increases significantly with the air compression ΔP and is predicted very close to the extrusion point, at a distance of 7–10 mm for each ΔP (Fig. 10). The negative pressure results from non-linear viscoelasticity of the polymer subjected to high elongation rates in the

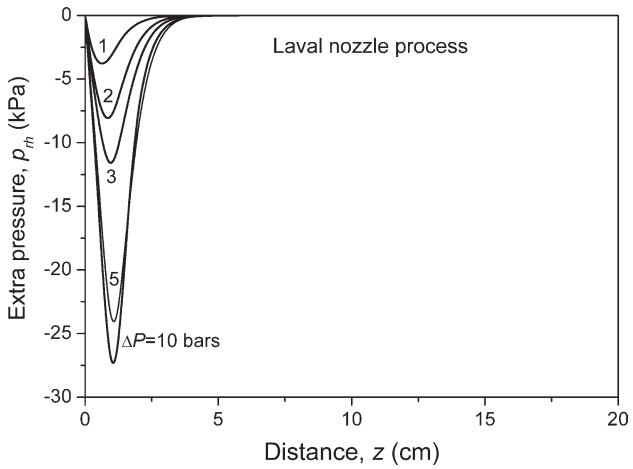

Figure 10 Extra-pressure p_{rh} in the iPP filament versus distance z predicted for the Laval nozzle process at several ΔP. Melt extrusion viscosity of 360 Pa s at 300°C (MFR = 12) and the collector located at $z = 20$ cm.

pneumatic process. It may cause cavitation in the polymer bulk which under uniaxial molecular orientation could lead to longitudinal burst splitting of the filament into a number of sub-filaments.

The cavitation under the influence of negative pressure (hydrostatic tension) is a usual cause in standard Newtonian fluids, but much less is known about this phenomenon in the case of polymer melts subjected to fast elongational flow such as in pneumatic drawing of melt filaments. Negative pressure induced cavitation in the polymer melts has been observed in the pockets of polyethylene, polypropylene, and poly(methylene oxide) melts occluded by impinging spherulites during polymer crystallization.[35,36] In this case, the negative pressure is buildup in the occluded melt due to change in density. Spontaneous formation of longitudinal cavities was observed by the real-time high-speed video microscopy at the exit of capillary die during extrusion of a linear polyethylene melt when the extensional stress at the die entrance exceeds a critical condition.[37] Numerical simulation of the stress fields in a capillary die predicted large negative pressure in a linear poly(dimethyl siloxane) melt near the exit region of the die.[38] It is postulated in Ref. 38 that the negative pressure cavitates polymer melt depending on the cohesion of the polymer bulk. Experimental observation of cavitation in polypropylene during tensile drawing led to the conclusion that initiation of the cavitation process in the amorphous phase has a homogeneous nature[39] and should depend on the cohesive forces in the melt.

With the assumption that the extra-pressure energy converts in total into the surface energy of sub-filaments during the hypothetical splitting at a point z_s of the axis, an average diameter of the sub-

filament created in the splitting should approximately read[13]

$$d(z_s) \cong -\frac{4\gamma(z_s)}{p_{\mathrm{rh}}(z_s)} \tag{25}$$

where γ is the surface free energy density of the polymer, and the extra-pressure is high enough, i.e., $-p_{\mathrm{rh}}(z_s) \gg 4\gamma(z_s)/D(z_s)$. Equation (25) is valid for the maximum absolute value of the extra-pressure predicted at the air compression $\Delta P > 1$ bar in the Laval nozzle, and the average diameter of the sub-filaments is controlled by the ratio of the surface free energy density and the negative extra-pressure. With this prediction, the sub-filament diameter in the supersonic process is controlled by the polymer surface tension. We assume temperature dependence of the surface free energy density of iPP melt $\gamma(z_s) = 2.94 \times 10^{-2} - 5.6 \times 10^{-5}\,[T(z_s) - 296]$ (in J/m^2).[34]

Average number of the sub-filaments predicted from such hypothetical splitting at z_s of an individual filament of diameter $D(z_s)$ reads,

$$N(z_s) = \left[\frac{D(z_s)}{d(z_s)}\right]^2 \cong \frac{1}{16}\left[\frac{D(z_s)p_{\mathrm{rh}}(z_s)}{\gamma(z_s)}\right]^2 \tag{26}$$

The predicted number of sub-filaments from the splitting under the extra-pressure taken at its maximum absolute value versus the air compression ΔP is shown in Figure 11 for iPP with the extrusion viscosity of 360 Pa s. Average diameter of the sub-filaments are indicated for the particular levels of splitting, from about 10 μm with splitting into 1000 sub-filaments at the air compression ΔP of 1 bar down to about 2 μm with spitting into 3000 sub-filaments above three bars. Saturation of the highest

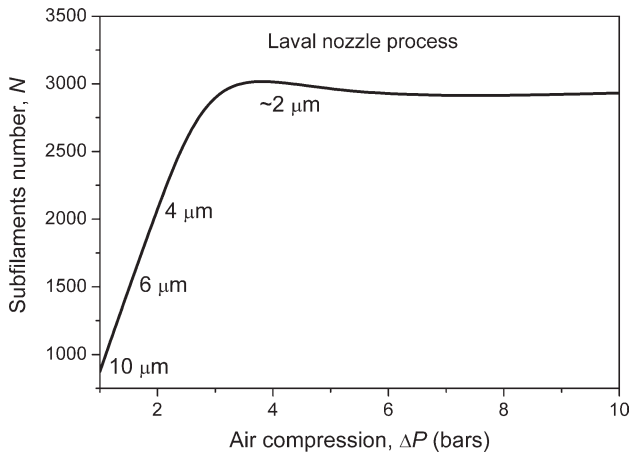

Figure 11 Average number N of iPP sub-filaments in the splitting versus air compression ΔP predicted for the Laval nozzle process. Melt extrusion viscosity of 360 Pa s at 300°C (MFR = 12) and the collector located at $z = 20$ cm. Average diameter of the sub-filaments indicated.

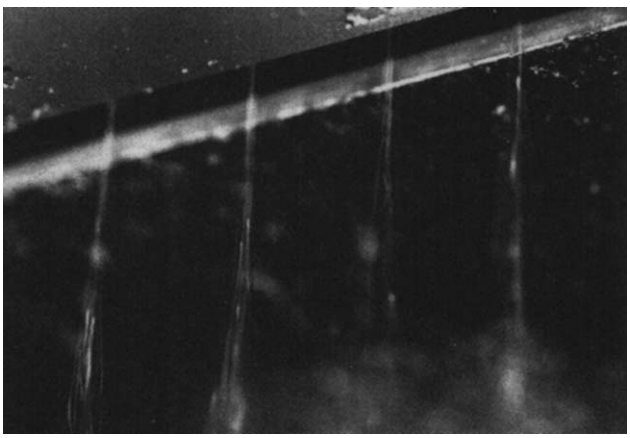

Figure 12 Splitting of polypropylene melt monofilaments in a Laval nozzle process registered by a photo at 1/8000 s. Re-printed from Ref. 6 by the courtesy of the Chemical Fibers International.

number and the lowest diameter of the sub-filaments is predicted above three bars of the air compression.

Splitting of air drawn filaments into super-thin sub-filaments in the supersonic Laval nozzle process was reported by Gerking[6] in the Nanoval process. Gerking claims that the photo in Figure 12 (re-print from Ref. 6) shows splitting of individual filaments into a bundle of sub-filaments taking place within the Laval nozzle range. In this range, we predict highest cavitation extra-pressure in the polymer bulk. Average diameter of the sub-filaments after the spitting measured in the Nanoval process[6] was in the range between 15 μm at the lowest splitting to about 2 μm at the highest number of sub-filaments in the splitting. Nevertheless, such a phenomena is controversial and has not been observed by other authors in the supersonic process where the finest filaments with a diameter of 10–20 μm and smooth surface were obtained without any evidence of filament splitting.[10,11]

CONCLUSIONS

Computer modeling of air-drawing of polymer melts in pneumatic melt spinning reduces to modeling of the predetermined two-dimensional fields of the air velocity, temperature, and pressure and one-dimensional stationary melt spinning by the coaxial air jet along its centerline. The model allows analysis of the air-drawing dynamics in the Laval nozzle process versus melt blowing and the role of individual processing and material parameters. Significant differences in the dynamics of both pneumatic processes result from the differences in the character of the air jets—supersonic and high-velocity jet over relatively long range of the process axis in the Laval nozzle method and fast decaying air jet in melt blowing, which results in highly coiled and entangled fibers

in the non-wovens. Contrary to melt blowing, air-drawing in the Laval nozzle extends over a long range of the process axis and allows to obtain continuous fibers by depositing them onto a collector as a non-woven, or winding-up by a drum. This feature opens possibilities of modifications of the supersonic process for obtaining high strength continuous filaments with high molecular orientation on the winder.

Strong influence of the air jet velocity, the die-to-collector distance, and the melt extrusion viscosity (MFR index) which controls response of the polymer melt on the air-drawing forces has been predicted from the modeling. Melt blowing is particularly sensitive to the collector position where the air-drawing zone is limited by the coiling. Influence of other processing parameters, such as initial air temperature, geometry of the air die, initial temperature of the polymer melt, extrusion velocity of the polymer, extrusion orifice diameter, can be also predicted.

The model predicts negative rheological extra-pressure which results from non-linear viscoelasticity of the polymer melt subjected to fast elongation in the pneumatic process. The pressure activates in the polymer bulk in a narrow range of the air-drawing axis inside the Laval nozzle and can lead to longitudinal cavitation under the orienting tensile stresses. Hypothetical burst splitting of the filament into a high number of sub-filaments is considered following an energetic criterion of transformation of the pressure energy into surface energy of the sub-filaments. The splitting is controversial nevertheless, and lack of the experimental data in the literature on the Laval nozzle process melt spinning process does not allow for verification of the model predictions. Validation of the modeling of the pneumatic air-drawing processes is given by comparison of the model predictions with the experimental data provided in the literature for melt blowing.

References

1. Bresee, R. R.; Ko, W.C. Int Nonwoven J 2003, 12 (Summer) 21.
2. Pinchuk, L. S.; Goldade, V. A.; Makarevich, A. V.; Kestelman, V. N. Melt Blowing: Equipment, Technology, and Polymer Fibrous Materials; Springer: Berlin, 2002.
3. Sen, A.; Badding, J. V.; Borkar, S.; Bin, G.; Dirmyer, M.; Delocado, R.; Jackson B. R. Polymer 2006, 47, 8337.
4. Ellison, C. J.; Phatac, A.; Giles, D. W.; Macosco, C. W.; Bates, F. S. Polymer 2007, 48, 3306.
5. Zhao, R. Int Nonwoven J 2002, 11 (Winter) 37.
6. Gerking, L. Chem Fibers Int 2002, 52, 424.
7. Gerking, L. Chem Fibers Int 2004, 54, 261.
8. Gerking, L. Chem Fibers Int 2005, 55, 52.
9. Stobik, M. Nonwovens World,2007, 16(2) Spring.
10. Lewandowski, Z.; Ziabicki, A.; Jarecki, L. Fibres Text Eastern Eur 2007, 15, 64.
11. Yao, D.; Wang, Y.; Jun, J. National Text Center Ann Rep, November 2007.
12. Jarecki, L.; Ziabicki, A. Fibres Text Eastern Eur 2008, 16 (5), 17.
13. Jarecki, L.; Ziabicki, A.; Lewandowski, Z.; Blim, A. J Appl Polymer Sci 2011, 119, 53.
14. Krutka, H. M.; Shambaugh, R. L.; Papavassiliou, D. V. Ind Eng Chem Res 2003, 42, 5541.
15. Wilcox, D. C. Turbulence Modeling for CDF (Computational Fluid Dynamics); DCW Industries, Inc.: California, 1984, pp 176–183.
16. Wilcox, D. C. AIAA J 1988, 26, 1299.
17. Wilcox, D. C. AIAA J 1988, 26, 1311.
18. Pope, S. B. Turbulen Flows; Cambridge University Press: Cambridge, 2000.
19. Roache, P. J. Verification and Validation in Computational Science and Engineering; Hermosa Publishers: Albuquerque, 1998.
20. Zachara, A.; Lewandowski, Z. Fibres Text Eastern Eur 2008, 16, 17.
21. Mohammadi, B.; Pironneau, O. Analysis of the K-Epsilon Turbulence Model; Wiley: Paris, 1994, pp 51–62.
22. Harpham, A. S.; Shambaugh, R. L. Ind Eng Chem Res 1996, 35, 3776.
23. Moore, E. M.; Papavassiliou, D. V.; Shambaugh, R. L. Int Nonwoven J 2004 13(Fall) 43.
24. Ziabicki, A. Fundamentals of Fibre Formation; Wiley: London, 1976.
25. Ziabicki, A.; Jarecki, L.; Wasiak, A. Comput Theoret Polymer Sci 1998, 8, 143.
26. Jarecki, L.; Lewandowski, Z. Fibres Text Eastern Eur 2009, 17, 75.
27. Zieminski, K. F.; Spruiell, J. E. Synth Fibers 1986, 4, 31.
28. Majumdar, B.; Shambaugh, R. L. J Rheol 1990, 34, 591.
29. Bansal, V.; Shambaugh, R. L. Ind Eng Chem Res 1998, 37, 1799.
30. Phan-Thien, N. J Rheol 1978, 22, 259.
31. Larson, R. G. Constitutive Equations for Polymer Melts and Solutions; Butterwoths: Boston, 1988, p 171.
32. Lee, J. S.; Shin, D. M.; Jung, H. W.; Hyun, J. C. J Non-Newtonian Fluid Mech 2005, 130, 110.
33. van Krevelen, D. W. Properties of Polymers; Elsevier: Amsterdam, 2000, p 86, 463, 469, 676.
34. Mark, J. E. Physical Properties of Polymers, Handbook; AIP Press: New York, 1996, p 424, 670.
35. Galeski, A.; Piorkowska, E.; Koenczoel, L.; Baer, E. J Polym Sci Part B: Polym Phys 1990, 28, 1171.
36. Nowacki, R.; Piorkowska, E. J Appl Polym Sci 2007, 105, 1053.
37. Son, Y.; Migler, K. B. J Polym Sci B Polym Phys 2002, 40, 2791.
38. Tremblay B. J Rheol 1991, 35, 985.
39. Rozanski, A.; Galeski, A.; Debowska, M. Macromolecules 2011, 44, 20.